Fuel 367 (2024) 131491

Contents lists available at ScienceDirect

Fuel

journal homepage: www.elsevier.com/locate/fuel

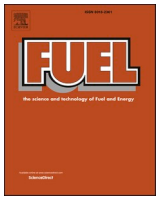

A laboratory study of secondary organic aerosol formation in an oxidation flow reactor

Fabio Sasso [a], Francesca Picca [a,*], Alessia Pignatelli [b], Mario Commodo [c], Patrizia Minutolo [c], Andrea D'Anna [a]

[a] Dipartimento di Ingegneria Chimica, dei Materiali e della Produzione Industriale, Università degli Studi di Napoli Federico II, Napoli 80125, Italy
[b] Dipartimento di Fisica, Università degli Studi di Napoli Federico II, Napoli 80125, Italy
[c] Istituto di Scienze e Tecnologie per l'Energia e la Mobilità Sostenibili, CNR, Napoli 80125, Italy

ARTICLE INFO

Keywords:
Particulate matter
Soot
Secondary organic aerosol
Size distribution
Mass-spectrometry

ABSTRACT

Secondary organic aerosol is formed through the atmospheric oxidation of gas-phase organic compounds and primary aerosols. Despite the potential risks that this class of particles poses to human health and climate, how primary emissions contribute to the formation of secondary organic aerosols remains largely unknown. This study examines the formation of secondary organic aerosols resulting from the oxidation of soot nanoparticles generated by a premixed laminar ethylene–air-rich flame. The exhaust gases and particles from the flame are conveyed into an oxidation flow reactor to simulate the atmospheric conditions in which secondary aerosol formation reactions occur. The pristine and oxidized aerosols are analyzed online using a scanning mobility particle sizer system to assess their size distributions. Moreover, collected aerosols are chemically characterized using a high-resolution time-of-flight aerosol mass spectrometer. The secondary aerosol formed exhibits an increase in mean diameter under different oxidation conditions and reveals an enhanced concentration compared to primary aerosols. These changes are accompanied by significant alterations in the chemical composition of the aerosols.

1. Introduction

Atmospheric aerosols have important implications for global warming, climate change, and human health [1]. Aerosols can influence the Earth's climate by a variety of effects. Reflecting incoming sunlight to outer space, aerosols have a cooling effect on the climate, while absorbing aerosols can trap energy within the atmosphere, thus warming the environment [2–4]. Moreover, toxicological and epidemiological studies have shown the multifaceted, detrimental health effects linked to aerosol exposure, e.g., cardiovascular, pulmonary, and cognitive [5,6], which are dominant factors in the millions of global deaths annually attributed to outdoor air pollution [7,8].

Despite the attention to atmospheric aerosol due to these strong effects on human well-being, its composition is not well known, and the mechanisms and the causes that enhance aerosol formation in the atmosphere are still controversial [9]. Despite the substantial advancements achieved in comprehending aerosol formation in the atmosphere, certain aspects of aerosol generation remain unclear. The uncertainty is due to the influences of diverse variables encompassing different precursor emissions, atmospheric chemistry, meteorological conditions, and interactions with other atmospheric constituents [10–12].

One significant component of atmospheric aerosol is organic aerosol (OA) which constitutes a substantial fraction of submicron aerosols worldwide [13,14]. The composition of organic aerosols (OAs) can be complex, encompassing thousands of compounds ranging from simple hydrocarbons to highly oxidized compounds [15,16]. Hydrocarbon components emitted directly are termed POA, while aerosols formed through the atmospheric oxidation of volatile and semi-volatile organic compounds (VOCs and S-VOCs respectively) are referred to as SOA [17,18]. Understanding the composition and sources of OA is essential for elucidating the mechanisms driving aerosol formation, including the contributions of primary and secondary aerosol precursors. Moreover, distinguishing between primary and secondary OA components provides insights into the relative importance of different aerosol formation pathways, contributing to the ongoing efforts to refine our understanding of atmospheric aerosol processes [19].

* Corresponding author.
E-mail address: francesca.picca@unina.it (F. Picca).

https://doi.org/10.1016/j.fuel.2024.131491
Received 1 January 2024; Received in revised form 5 March 2024; Accepted 14 March 2024
Available online 20 March 2024
0016-2361/© 2024 The Author(s). Published by Elsevier Ltd. This is an open access article under the CC BY license (http://creativecommons.org/licenses/by/4.0/).

OA is generally separated into hydrocarbon-like OA (HOA), oxygenated-like OA (OOA), and sometimes other primary components. HOA and OOA can be considered good surrogates for primary OA (POA) and secondary OA (SOA), respectively [17,19–21].

SOA in the environment comprises a significant and variable fraction (60–95 %) of OA [18], and it is believed to be formed via the atmospheric oxidation of gas-phase organic compounds, e.g., VOCs and S-VOCs [22,23], of both biogenic and anthropogenic origin. These oxidation reactions are mediated by reactive species such as ozone (O_3), nitrate (NO_3), and hydroxyl radicals (OH) under atmospheric conditions and transform compounds into less volatile products, some of which may undergo further reactions or partition into the condensed phase, thereby contributing to the complex chemical composition observed within aerosol particles [24].

Among anthropogenic activities influencing SOA formation, a key contribution at the urban scale is attributed to on-road and off-road vehicles [22] which are a significant contributor to both urban air particulate matter and gaseous pollution [25]. The considerable variability in emission rates and composition among vehicles and vehicle types, attributable to factors such as vehicle class, size, fuel type, operation mode, model year, and engine/post-combustion control technology, underscores the complexity of understanding vehicle emissions [26]. Moreover, differences in regulations between on– and off-road vehicles further compound this complexity.

Despite the recognized danger posed by these particles, particularly in the context of secondary organic aerosol formation, our comprehension of the underlying chemical and physical processes governing SOA formation and their resultant properties remains limited [27–30]. Several approaches have been used to characterize SOA, meant as a mixture of organic compounds emitted from fuel combustion. Estimation methods include top-down approaches, based primarily on ambient air quality measurements, and bottom-up processes focusing on the in-depth characterization of emissions [31,32]. The bottom-up approach consists of the oxidation of fresh exhaust from the combustion system in environmental chambers or oxidation reactors to simulate potential SOA formation in the ambient atmosphere [33]. In this study, this second approach was adopted.

Environmental chambers typically consist of several cubic meters in volume and are made by Teflon film, stainless steel, or Pyrex (borosilicate glass). These chambers serve to replicate atmospheric conditions within a controlled laboratory environment. They are often equipped with a standard array of instruments, including integrated temperature and humidity probes, as well as a differential pressure indicator. In these chambers, precursor gases and aerosols are introduced into the system. By employing specific light sources, such as natural sun-light [34], xenon arc lamps [35], and UV black lights [36], and oxidizing agents, researchers can handle the oxidation conditions within the chamber and simulate various atmospheric scenarios [37–39]. Conversely, oxidation flow reactors, OFR, are designed to generate highly oxidative environments, significantly expediting chemical processes that typically occur over several days in the atmosphere to mere minutes within laboratory or field settings [40]. Using an oxidation flow reactor instead of a large environmental chamber provides multiple advantages: shorter residence time, reduced wall losses, higher oxidation rate, and enhanced portability. Because of the reduced residence time, it is also possible to measure SOA formation of a changing emission source in real time [33,41,42].

In atmospheric chemistry research, OFR185 and OFR254 modes, i.e., OFR utilizing 185 nm and 254 nm photolysis lamps respectively, represent fundamental operational configurations widely employed for accelerated experimentation [43]. OFR254 mode employs filtered low-pressure mercury lamps to emit 254 nm light, facilitating the photolysis of externally supplied O_3 within the reactor to generate OH radicals. Conversely, in OFR185 mode, the low-pressure mercury lamps emit unfiltered 185 nm light capable of photolyzing H_2O molecules to produce OH radicals, and converting O_2 to O(3P), eliminating the necessity for externally supplied O_3 [33].

In this study, an OFR254 was utilized to investigate the formation of SOA from the oxidation of the products of incomplete combustion of ethylene in a fuel-rich laminar premixed ethylene–air flame. Ethylene was selected since this is a key intermediate in the combustion of hydrocarbon and its combustion behavior is thus representative of more complex hydrocarbon fuels used in combustion processes. Studying ethylene under fuel-rich conditions allows for the investigation of non-ideal combustion systems, such as those encountered in real-world combustion devices like on-road and off-road vehicles, industrial furnaces, residential heating appliances, and power plants. Indeed, also in clean combustion systems, local non-ideality occurs resulting in a complex ensemble of unwanted volatile and semi-volatile compounds, and particles with a broad range of size distribution ranging from a few nanometers to microns. The use of a laminar premixed flame reactor allows to selectively simulate the formation of single classes of these compounds typically found at the exhaust of real systems by the proper choice of the flame parameters such as temperature and fuel/oxidant composition and reaction time. Indeed, in this flame, the height above the burner is representative of the reaction time thus flame products sampled at different points in the flame are representative of different stages of formation and growth.

The products of incomplete combustion, including NOx, VOC, mono- and polycyclic aromatic hydrocarbon (PAH) compounds, and soot nanoparticles, were collected at different residence times in the flame and convoyed to an oxidation flow reactor which simulates the conditions that combustion exhausts find in the atmosphere. A scanning mobility particle sizer (SMPS) and a high-resolution – time of flight – aerosol mass spectrometer (HR-ToF-AMS) were also used to follow the evolution of the particles' size distributions (PSD), the nucleation of new particles and chemical composition variations of the combustion products in an environment which mimics the atmospheric transformation.

2. Experimental procedure

2.1. Combustion system/apparatus

An atmospheric pressure laminar premixed ethylene–air flame, operating under fuel-rich conditions, was used to produce products of incomplete combustion. The flame was stabilized on a water-cooled sintered steel McKenna burner with a diameter of 6 cm. The cold gas velocity was set at 9.8 cm/s, and the carbon to oxygen (C/O) atomic ratio at 0.67 (equivalence ratio, $\phi = 2.01$).

For all the investigations, the combustion products were extracted from the flame centerline through a tubular dilution probe, as described in previous studies [44–46]. The combustion products were collected at different heights above the burner (H), representing different residence times in flame. In this work, the H was fixed at 8, 10, and 14 mm, representing three different regions of the soot formation process, particle nucleation ($H = 8$ mm), early particle growth ($H = 10$ mm), and particle maturation/carbonization ($H = 14$ mm), respectively [47].

2.2. Oxidation flow reactor

A detailed representation of the experimental set-up is represented in Fig. 1. The sampled gaseous flame products and particles were convoyed to an oxidation flow reactor developed by Dekati® (DOFR^{TM}) where an oxidation process is performed via ozone-generated OH radicals [33] (see Supplemental Material for a more detailed description).

Different amounts of ozone and water molecules allow mimicking different residence times in the atmosphere, thus following the aerosol aging time from a few hours up to a few days. Some details about the correlation between ozone concentration and atmospheric aging times are reported in the supplementary material. At the exit of DOFR^{TM} the generated aerosol particles are analyzed through online and offline measurements by SMPS and HR-ToF-AMS, respectively.

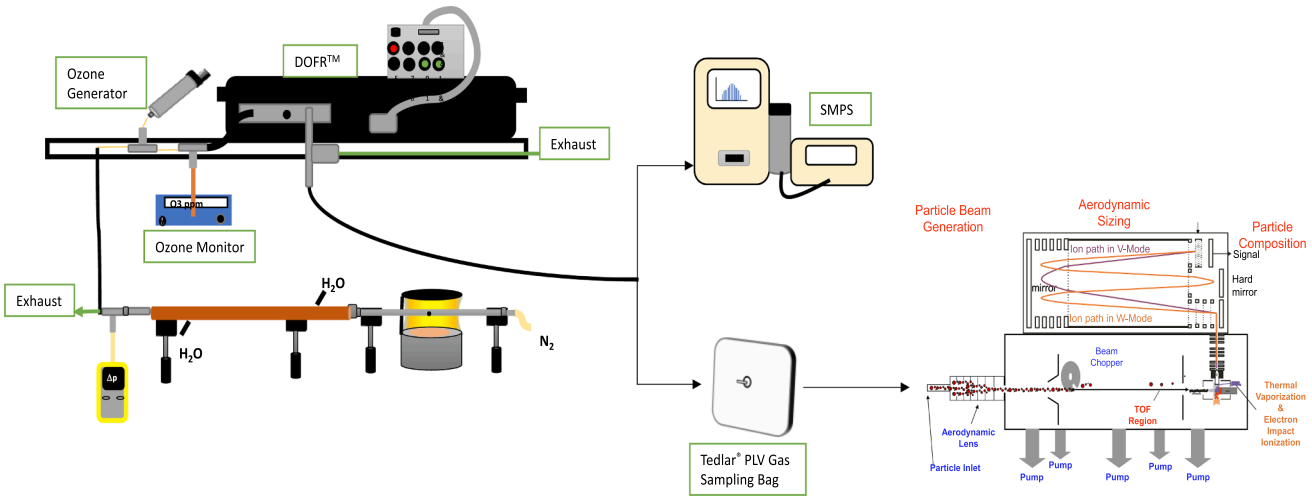

Fig. 1. Experimental set-up.

2.3. On-line and off-line measurements: SMPS and HR-ToF-AMS

Particle size distributions (PSDs) were measured online by an SMPS system positioned at the exit of the DOFR™. To collect flame products, a turbulent flow tubular dilution probe, positioned horizontally to the flame was used; the probe consists of a tube with a 1 cm outer diameter with an orifice (ID = 0.2 mm, thickness = 0.5 mm) for sampling; it uses N_2 as diluent ensuring a dilution ratio, *DR*, of $1:3 \bullet 10^3$ [44–46]. Such a sampling procedure was adopted to prevent particle coagulation and to quench chemical reactions, thus avoiding particle mass growth within the sampling line. The aerosol flow containing particles and unburned species is then sent to an Advanced Aerosol Soft X-ray Neutralizer, model TSI 3088. This process aimed to achieve Fuchs' stable charge distribution [48]; subsequently, the particles and unburned species are selected with a cylindrical electrostatic classifier by differential mobility analysis (DMA), model TSI 3085 and counted by a Condensation Particles Counter (CPC), model TSI 3776. TSI aerosol instrument manager software (AIM) was used to determine the particle size distribution function. Furthermore, the Multi-instrument manager software accounts for the particle losses inside the instrument by diffusion to the walls and applies correction for multiple charges. In a post-processing analysis, a total sampling efficiency was calculated and applied to the data [49].

Flame products' composition was analyzed offline by a HR-ToF-AMS (from Aerodyne Research. Inc. ARI). To this aim, samples were collected in 5L Tedlar® PLV Gas Sampling bags, which are usually employed for sampling of gas and are also suitable to collect emissions from combustion chamber [50]. HR-ToF-AMS is equipped with a $PM_{2.5}$ aerodynamic lens which enables particles of about 100 nm [51] to be detected with a great efficiency. Therefore, it was necessary to allow the coagulation of particles to enable their detection by the HR-ToF-AMS. This was achieved using a probe with a larger orifice diameter than that used for SMPS measurements, i.e., 2.5 mm instead of 0.2 mm. The dilution ratio obtained with this probe was *DR* = 1:21, high enough to quench flame reactions and reduce chemical modification of the collected material, but low enough to allow particle coagulation. The relative cumulative size distributions are reported in Fig. S2.

Particles collected in the Tedlar® sampling bags were analyzed by an HR-ToF-AMS, enabling fully molecular-resolved online quantification of organic aerosol [52]. Aerosol particles are sampled from the bag through the $PM_{2.5}$ aerodynamic lenses and focused into a narrow beam that impacts a resistively heated (ca. 600 °C) capture vaporizer, where the non-refractory particle species are vaporized. The resulting vapors are then ionized by a 70-eV electron beam and convoyed into the mass spectrometer for analysis. In addition, HR-ToF-AMS is also equipped with the Soot Particle AMS (SP-AMS) for detecting refractory particle species such as Black Carbon and metals. A detailed description of the HR-ToF-AMS, SP-AMS, and the operating conditions is reported in the supplemental material.

The acquired data were analyzed with the ToF-AMS analysis toolkit Squirrel 1.65/PIKA 1.25 version provided by Aerodyne Research Inc. Details of the software's analysis are described in DeCarlo et al. [53]. The acquisition of the data through the AMS allows to evaluate Unit Mass Resolution (UMR) spectra up to a chosen *m/z* (fixed at 1100 in this study) and simultaneously analyse the signals between 12 and 120 *m/z* with a mass resolving power up to 2500 (high-resolution region). A comprehensive elucidation of the data processing and the derived informational content from the HR-ToF-AMS can be located within the corresponding section of the supplementary materials. In this study, a detailed analysis of the main chemical compounds present in samples was performed; a tracers investigation as indicators of POA and SOA, the triangular plot, and the Van Krevelen diagram to study the evolution of aerosols within the oxidation processes, are reported.

3. Results and discussion

3.1. Particle size distributions

The PSDs measured at the three flame sampling locations are reported in Fig. 2. The plot reports the PSDs measured at the exhaust of the DOFR™ with and without the ozone addition, 0 ppm and 5 ppm respectively. Information about the aging time corresponding to 5 ppm of O_3 are reported in Fig. S1 in the supplemental material.

At 8 mm, Fig. 2.a, the particles produced in the flame are smaller than 10 nm and the size distribution is unimodal. The activation of photo-oxidation reactions by ozone induces the formation of new and larger particles and PSD presents two additional modes centered at about 8 nm and 30 nm respectively. A similar behavior is observed at 10 mm, a slight increase in the particle mode centered at about 8 nm, and the formation of the new mode of particles larger than 15 nm, Fig. 2.b. At 14 mm, Fig. 2.c, another effect is highlighted: an additional mode with particles of intermediate size equal to 6 nm is observed when photo-oxidation is induced. The effect is highlighted in Fig. 3 where the PSDs of the particles after 2 days of aging ($[O_3]$ = 5 ppm) due to the photo-oxidation of incomplete combustion products at different residence times, are reported.

This new particle mode is observed particularly at 14 mm and could be attributed to soot particle oxidation-induced fragmentation [54,55]. The chemical characterization of this particle mode could help in understanding the origin.

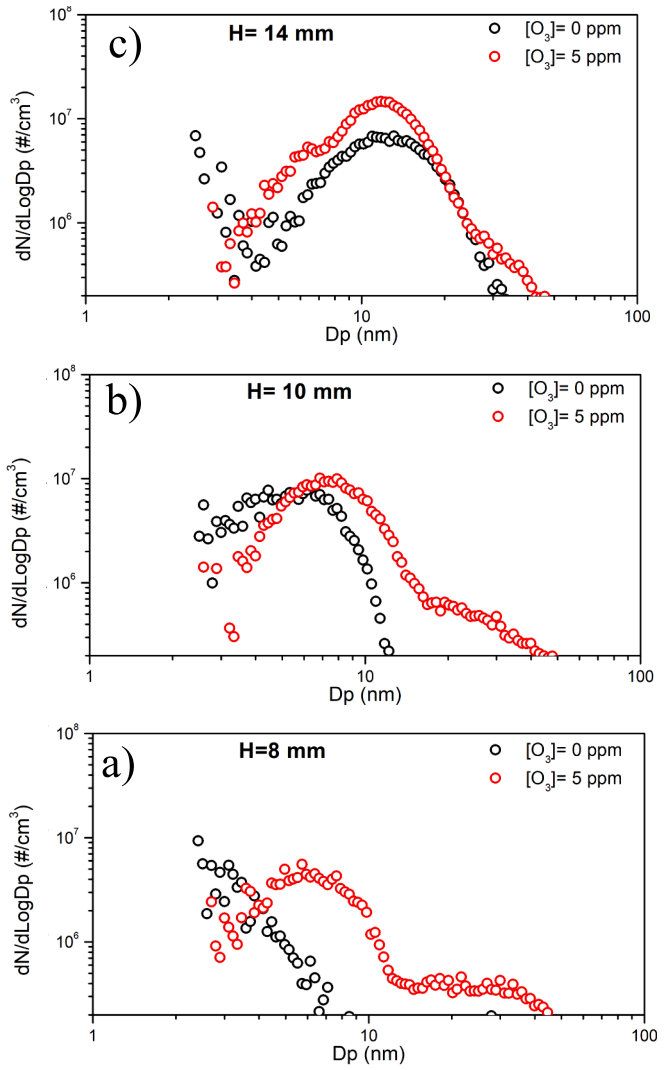

Fig. 2. Particle size distribution (PSD) at different flame conditions: a) $H = 8$ mm; b) $H = 10$ mm; c) $H = 14$ mm, measured at the exit of the DOFR^{TM} reactor with and without ozone.

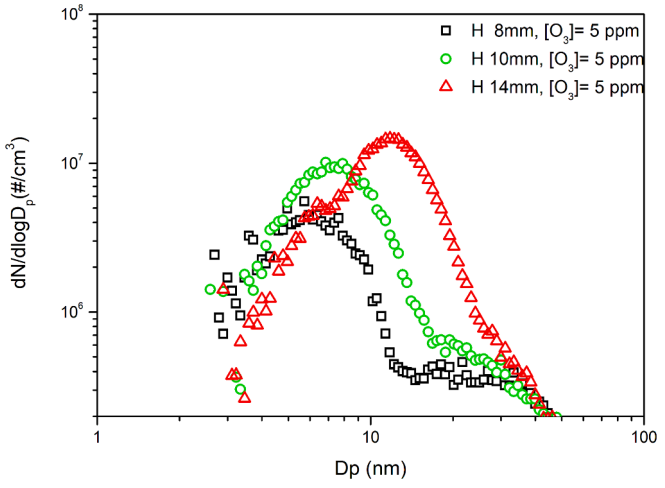

Fig. 3. PSDs at the three-residence time considering only one oxidation condition, i.e., 5 ppm ozone concentration.

3.2. Unit mass resolution (UMR) AMS profiles

The mass spectra of the incomplete combustion products collected at 8, 10, and 14 mm above the flame have been analyzed by HR-ToF-AMS. Fig. 4 reports the mass spectra of 0 and 5 ppm of ozone concentration for the three *Hs*, in the 100–1100 *m/z* range. The upper diagrams report the oxidized conditions (5 ppm), and the lower plots describe the no-oxidized conditions (0 ppm).

The reported spectra are relative to the entire exhausted compounds, including gases and particulate matter. Molecular masses span over the entire investigated range, with the most intense peaks falling in the 100–600 *m/z* range. Several PAHs of moderate size (about the size of coronene to ovalene) are present and even a series of peaks attributed to pure carbon species (C_x), i.e., fullerenes structures, in the 14 mm sample mass spectrum are noticed. This outcome aligns with the results reported by Sabbah et al. [47] in a comparable flame operating sooting condition, where two-step laser desorption ionization mass spectrometry (LDI MS) was employed as the mass spectroscopic technique.

A preliminary analysis of the spectra highlights that, by photo-oxidation of the samples, most of the PAH peaks disappear. Indeed, a reduction of the peaks is observed in the *m/z* range from 300 to 500 for the three *Hs* equal to 8, 10, and 14 mm, indicating that these species participate in oxidative processes. Furthermore, particularly at the highest *H*, a reduction is also observed for the peaks registered in the *m/z* range 700–1000. Simultaneously, there is a notable increase in the overall signal detected in the oxidizing conditions, indicating the potential nucleation of new particles. In particular, for $H = 8$, 10, and 14 mm, under oxidized conditions, we observe an increase in the total ion signal of 12 %, 17 %, and 18 %, respectively.

3.3. High-resolution (HR) AMS profiles

The effects of photo-oxidation can be better explained by studying the organic spectra in the lower mass region which has a higher mass resolution [21,53,56]. Electron impact at 70-eV is a very fast, sensitive but also harsh ionization technique that results in fragmentation of the input species [57]. Within the mass region of 12–120 *m/z*, approximately 82 to 90 percent of the signals in each sample falls, enabling a more precise examination of the elemental composition of the aerosol.

The high-resolution mass spectra (HR-MS) in Fig. 5 followed a fitting procedure performed by PIKA software, resulting in a peak separation by fragment ions with a mass resolving power up to 2500 in the *m/z* range of 12–120 [53]. These fitted ions have been grouped according to the molecular composition in seven families: C_x, CH, CHO_1, CHO_{gt1}, CHN, CHO_1N, and $CHO_{gt1}N$ (where O_{gt1} stands for number of oxygen atoms greater than one). We have chosen these families in the HR analysis according to the chemical composition of the species present in the flame-formed aerosols where we expect purely carbon, hydrogen, oxygen, and nitrogen atoms. This family subdivision provides insights into the composition of the aerosol before and after the effects of photo-oxidation. It is crucial to highlight that, to obtain a clearer analysis of the organic fractions, we deliberately excluded the $C_2H_4^+$ ion from the fitting process because the ion $C_2H_4^+$ has a mass-to-charge ratio close to that of N_2 (28.03130 vs. 28.00615) and the software is unable to provide an accurate evaluation of these two species.

In Fig. 5 pie charts are also reported, indicating the percentage contribution of each family. The CHON and $CHO_{gt1}N$ families have minor contributions in all the displayed spectra. The combined sum of CHON and $CHO_{gt1}N$ is less than 5 % for both unoxidized and oxidized samples. As expected, the CH family consistently represents the largest contribution. Increasing the height above the burner, the CH fraction tends to increase because, as the concentration of ethylene (not included in the ion fitting procedure) decreases, the other species in the family become more predominant. The contribution of the C_x family also follows the increasing pattern along *H* observed above in the spectra at wider *m/z* ranges. This trend was also reported in the study performed

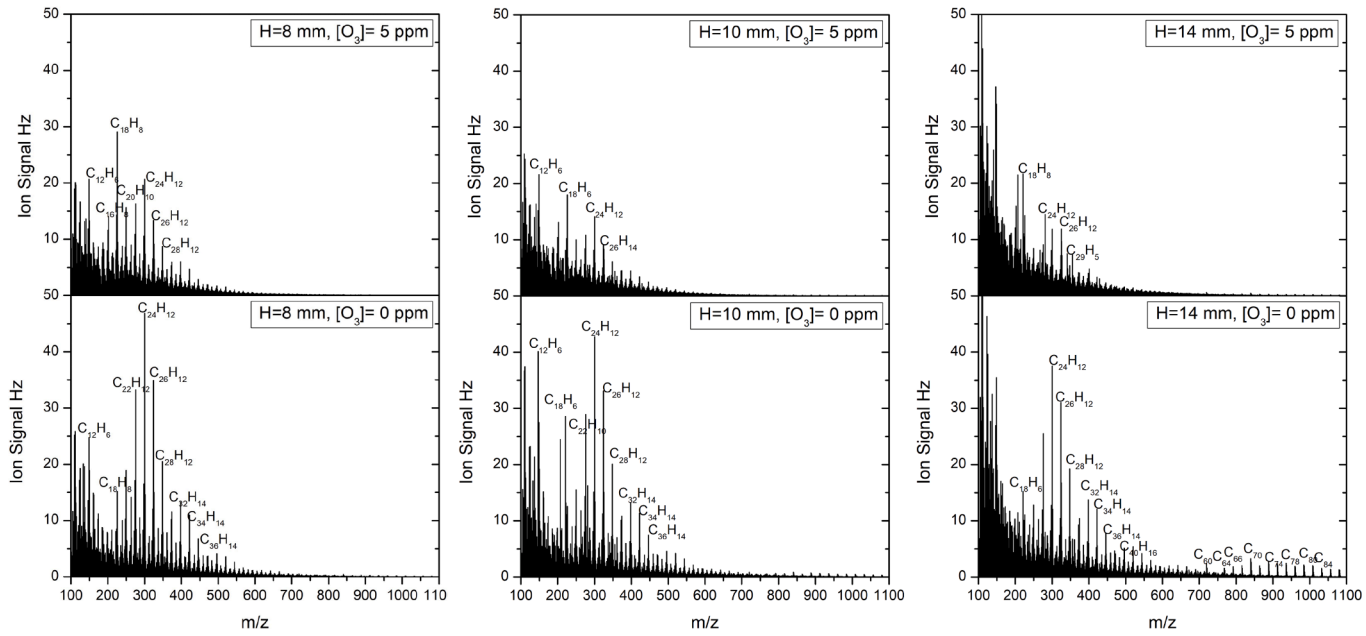

Fig. 4. Mass spectra of unburned gas. From left to right, $H = 8$ mm, 10 mm, 14 mm. Upper side: ozone concentration of 5 ppm Lower side: without oxidation. The main peaks report the labels related to the chemical species contributing to the signals.

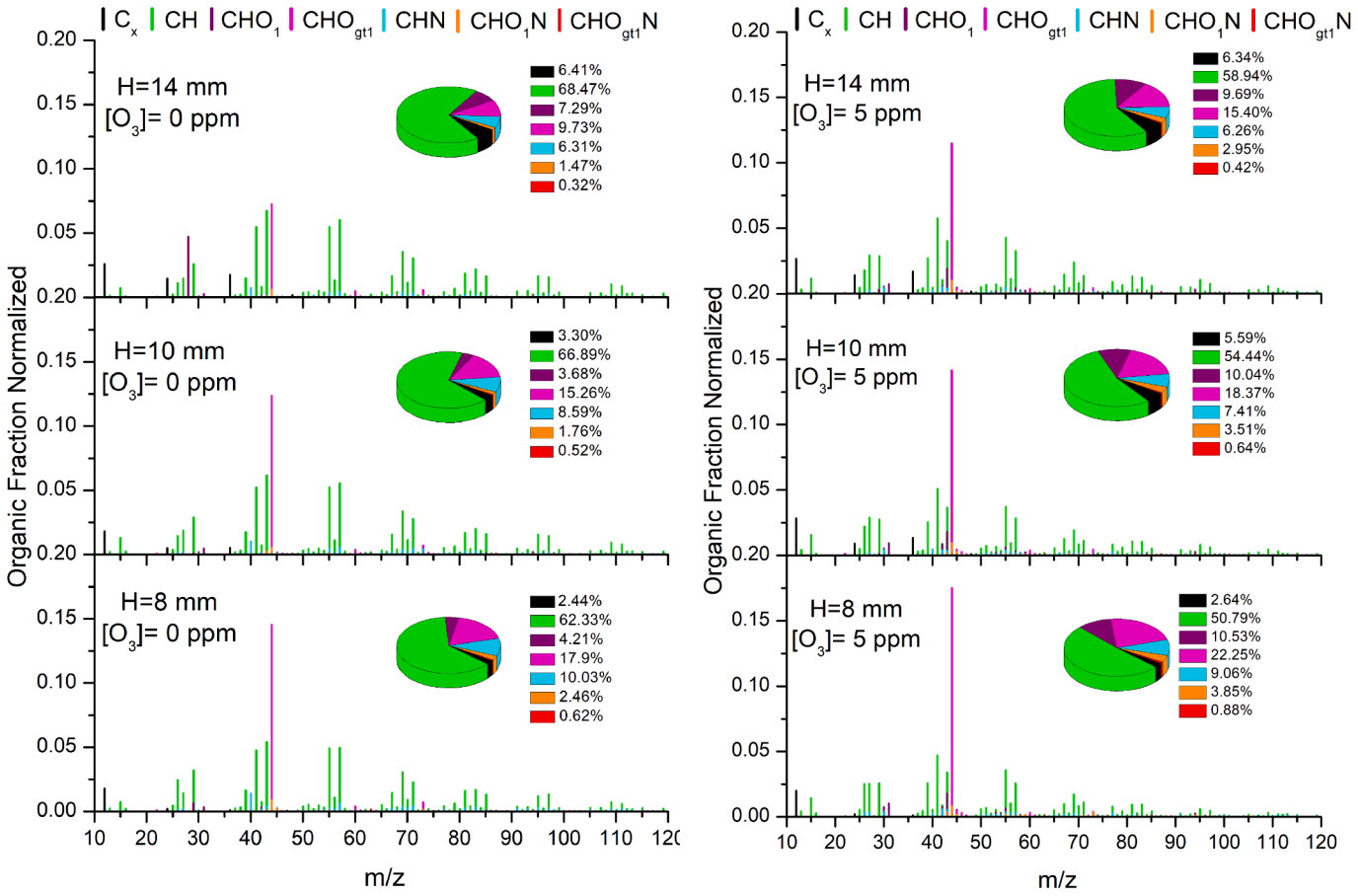

Fig. 5. The high-resolution mass spectra profiles subdivided into the main chemistry family whose relative distributions are shown in the pie chart inserts. On the left, the acquisition for samples at no-oxidation conditions; on the right, the acquisition for samples at 5 ppm ozone concentration.

by Sabbah et al [47]. The effects of photo-oxidation are noticeable since the oxygenated CHO and CHO_{gt1} families exhibit an increased contribution following the oxidation process.

It also appears that under shorter residence times in flames, species with a higher tendency to react within the oxidation chamber are generated, resulting in a higher concentration of oxygenated

compounds. Indeed, at $H = 8$ mm, the CO_2^+ ion related to the m/z 44 exhibits the highest proportion of oxidized hydrocarbons, representing the largest peak at 17.5 % of the HR-MS. In addition, the peak at m/z 43 also shows the effects of photo-oxidation due to the presence of the $C_2H_3O^+$ fragment.

The effect of photooxidation becomes even more evident in the plots presented in Fig. 6, where differences in the signals of high-resolution ions between SOA ($[O_3] = 5$ ppm) and POA ($[O_3] = 0$ ppm) are depicted. Negative signals correspond to species, for each specific m/z, that contribute more to the POA; conversely, positive signals correspond to species that contribute more to the SOA. Therefore, for each family, it is possible to identify the components that contribute to the specific m/z signal. Significant variations are observed, particularly within the CHO_{gt1} and CH families, enabling us to hypothesize which class of species are more prominently involved in oxidative processes and consider them tracers of the phenomena.

A detailed analysis of the tracers shows that among the CHO and CHO_{gt1} families, represented in Fig. 6 by purple and magenta columns respectively, the following m/z ratios, 43, 44, 45, 46, and 47 show the strongest increase after the oxidation process. The increment can be noticed for all the flame heights. These m/z values are associated, by the HR analysis, with specific fragments: $C_2H_3O^+$ (43.01839 m/z), CO_2^+ (43.98938 m/z), CHO_2^+ (44.99760 m/z), $CH_2O_2^+$ (46.00548 m/z) and $CH_3O_2^+$ (47.01330 m/z). Furthermore, among the CH family, represented in Fig. 6 by green columns, the strongest decrement is observed for the following m/z: 43, 55, 57, 69, 71, 83, 85. As for the previous case, the same trend is noticed for each height. Again, the HR analysis allows to associate these m/z to the specific fragment contribution: $C_3H_7^+$ (43.05470 m/z), $C_4H_7^+$ (55.05030 m/z), $C_4H_9^+$ (57.07043 m/z), $C_5H_9^+$ (69. 07043 m/z), $C_5H_{11}^+$ (71.08606 m/z), $C_6H_{11}^+$ (83.08606 m/z), $C_6H_{13}^+$ (85.10172 m/z). Coherently with the literature analysis, an increment of the oxidized species and a decrease in the hydrocarbon-like structures are registered due to the application of photo-oxidation [20,58,59]. In this sense, a more detailed analysis is presented in the following paragraph, where an investigation of specific tracers of the photo-oxidation process is performed.

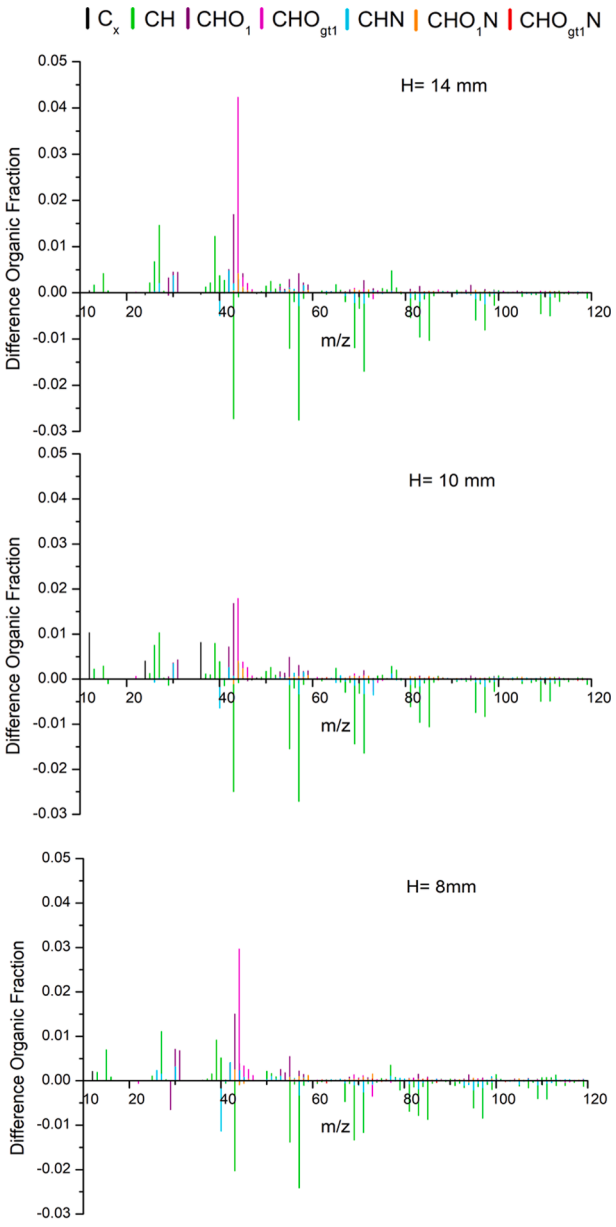

Fig. 6. Differences in the HR-MS signals of ions between SOA and POA.

3.4. Characteristics of tracers in HR-ToF-AMS

Tracers can be a useful tool for the mass spectra interpretation. Following the analysis described in the supplemental material, AMS data processing section, the trends of various m/z ratios related to literature-known tracers are proposed. All the m/z ratios associated with carbonaceous compounds that have been investigated are reported in the tables below: Table 1 and Table 2, which summarize the HOA and OOA, respectively. All the values are referred to the organic fraction normalized reported in Fig. 5. All the conditions, in terms of height above the burner and ozone concentration, have been considered for the comparison. Next to the m/z values, the most probable chemical species [53] is highlighted in the second column of the two tables. Regarding the HOA tracers, a notable decrease from the non-oxidated to oxidated conditions is observed for the following mass-to-charge ratios: 57, 67, 69, 71, 81, 83, 85, 95, and 97 m/z. Zhang et al. [20] associated these mass-to-charge values to hydrocarbon-like species, in the generic form of CH. By increasing the photo-oxidation processes, their signals tend to decrease for each H [20].

In Fig. 7, the histogram plots reporting the relative abundance of the m/z equal to 15, 44, 85, and 97 for the various analyzed conditions are shown. The trends of two representative m/z ratios for the HOA (hence for POA) are reported in Fig. 7.a and 7.b, corresponding to m/z 85 and 97; these two signals were chosen because, among the various m/z ratios, their decrement is more pronounced. Zhang et al. [20] associated these values to $C_6H_{13}^+$ and $C_7H_{13}^+$, respectively. These hydrocarbon-like structures with a considerable carbon chain tend to suffer oxidative conditions. Therefore, for each H, the signals associated with these hydrocarbon-like molecules decrease in the oxidized case. The same analysis was performed for the OOA tracers. The OOA tracers, used as SOA indicators exhibit specific m/z, including 15, 17, 18, 31, 44, 45, 53. For these m/z ratios, and each H, an increase is observed when moving from non-oxidized to oxidized conditions. As an example, two signals are reported, m/z 15 and 44 in Fig. 7.c and Fig. 7.d, respectively. The first signal, m/z equal to 15, is commonly associated with the presence of methyl radical, CH_3^+ [60]. This radical can be produced by the fragmentation of aromatic-like structures which could be more and more affected by the increased oxidative conditions [20,58]. On the other hand, the m/z 44 is associated with the CO_2^+ ion presence, generally considered a marker of a sample's oxidation level [21]. As for m/z 15, an increase for each height above the burner is registered.

3.5. Triangular plot and Van Krevelen diagrams

In Fig. 8, the so-called "triangular plot", i.e., the results of the *f*43 vs. *f*44 analysis, is reported. The fractions *f43* and *f44* represent the ratio of m/z 43 and m/z 44 to the total organic signal, respectively. The m/z 43 serves as an indicator of saturated carbonyl groups, although it can also

Table 1
Mass-to-charge ratios of the main HOA tracers reported as organic fraction normalized signals.

HOA *m/z*	Fragment	*H* = 8 mm		*H* = 10 mm		*H* = 14 mm	
		0 ppm	5 ppm	0 ppm	5 ppm	0 ppm	5 ppm
57	$C_4H_9^+$	0.0572	0.0329	0.0621	0.0354	0.0658	0.0397
67	$C_5H_7^+$	0.0178	0.0129	0.0181	0.0156	0.0195	0.0173
69	$C_5H_9^+$	0.0345	0.0219	0.0374	0.0234	0.0394	0.0270
71	$C_5H_{11}^+$	0.0280	0.0163	0.0333	0.0170	0.0345	0.0186
81	$C_6H_9^+$	0.0189	0.0123	0.0195	0.0130	0.0209	0.0153
83	$C_6H_{11}^+$	0.0215	0.0140	0.0241	0.0143	0.0251	0.0154
85	$C_6H_{13}^+$	0.0142	0.0079	0.0177	0.0082	0.0201	0.0100
95	$C_7H_{11}^+$	0.0158	0.0087	0.0174	0.0098	0.0184	0.0122
97	$C_7H_{13}^+$	0.0163	0.0076	0.0178	0.0085	0.0193	0.0099

Table 2
Mass-to-charge ratios of the main OOA tracers reported as organic fraction normalized signals.

OOA *m/z*	Fragment	*H* = 8 mm		*H* = 10 mm		*H* = 14 mm	
		0 ppm	5 ppm	0 ppm	5 ppm	0 ppm	5 ppm
15	CH_3^+	0.0075	0.0145	0.0129	0.0157	0.0073	0.0115
31	CH_3O^+	0.0035	0.0104	0.0051	0.0095	0.0027	0.0073
44	CO_2^+	0.0179	0.0279	0.0141	0.0281	0.0120	0.0249
45	CO_2H^+	0.0060	0.0096	0.0041	0.0088	0.0023	0.0089
53	C_3HO^+	0.0065	0.0106	0.0063	0.0099	0.0064	0.0098

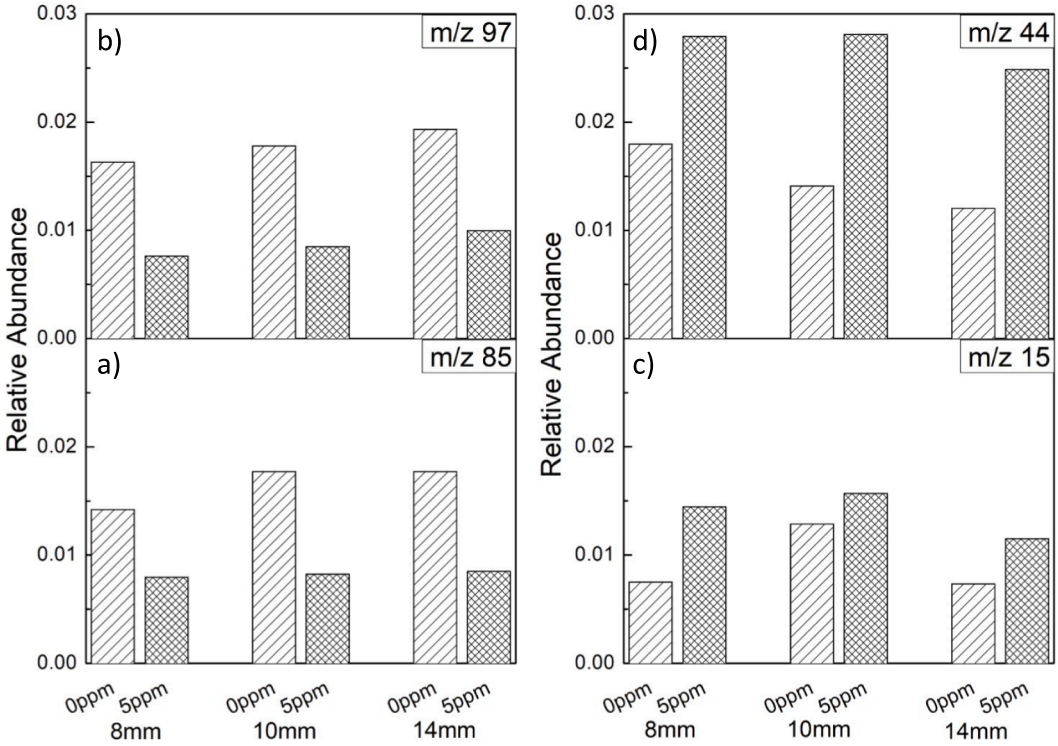

Fig. 7. Relative abundance of different *m/z* ratios at different flame heights at 0 ppm and 5 ppm. For HOA: a) *m/z* equal to 85; b) *m/z* 97. For OOA tracers: c) *m/z* 15; d) *m/z* 44.

originate from other types of species. The *m/z* 44 is attributed to the CO_2^+ signal due to the thermal decarboxylation of oxo-, di-, and poly-carboxylic acids [57,61,62]. The red and blue dashed lines, reported in the plot, delimit the triangular region where atmospheric samples of SOA components generally fall [63]. A detailed description of the triangular plot is reported in supplemental material.

Under non-oxidation conditions, a rise in flame residence time leads to observable trends: a decrease in *f*44 and an increase in *f*43. These trends are in alignment with the data presented in the pie chart of Fig. 5. Therefore, higher flame residence time impacts on an increase in the fraction of hydrocarbon species. In an oxidation environment, a similar trend is observed, but with higher values for the *f*44. This result indicates the occurrence of an oxidation process, resulting in the generation of organic oxygenated carboxylic species. The *f*43 of samples subject to oxidation environment remains relatively constant when compared to the $[O_3] = 0$ ppm condition. This suggests that the photo-oxidation process promotes the formation of oxygenated compounds while simultaneously reducing hydrocarbon-like species. This

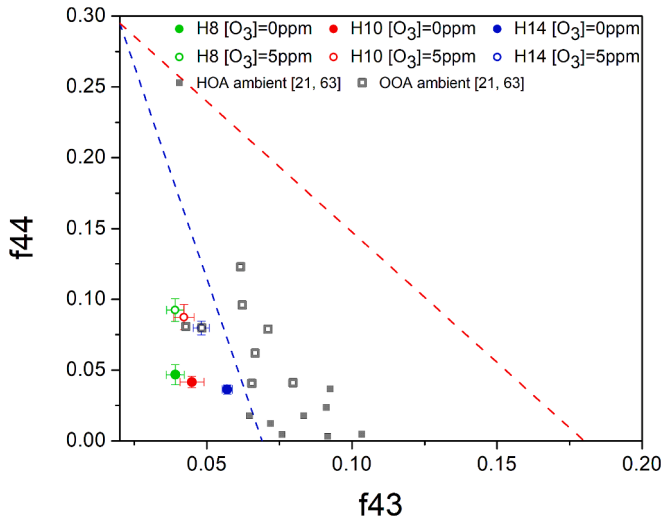

Fig. 8. Triangular plots showing both ozone concentrations, i.e., 0 and 5 ppm. In the diagram, the HOA and the OOA ambient data provided by Ng et al. [21,63] are also reported. The grey full squares represent the HOA components, while the green empty squares represent the oxygenated OOA components.

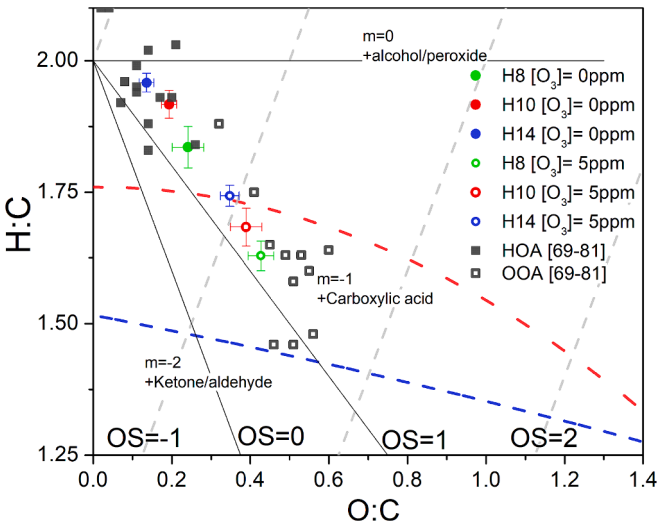

Fig. 9. Van Krevelen plots reporting both 0 and 5 ppm ozone concentration the H:C and O:C data of the ambient components provided by Canagaratna et al. [68] are also reported. The grey full squares represent the hydrocarbon-like organic aerosol (HOA) components, while the grey empty squares represent the semi-volatile oxygenated organic aerosol (SV-OOA) components. The straight black lines, labeled as "m", separate different regions in which the main oxygenated functional groups are located. Different OSs are represented on the plot by the positive-slope grey dashed lines. The blue and red dashed lines indicate the lower and the upper limits of the region where atmospheric samples of SOA generally fall.

observation aligns with the findings in Fig. 5, as detailed in Section 3.3 of the study. Notably, it is worth mentioning that in both cases, the data points fall outside the defined triangular zone. The results presented in Fig. 8 were compared with literature data [21,63], in which the organic aerosol components were determined through a multivariate factor analysis of datasets in the UMR of the Northern Hemisphere. The oxidized products of our study appear consistent with the environmental OOA reference data. Indeed, under unoxidized conditions, our samples show a lower *f44* value than the corresponding oxidized samples, which is consistent with the *f44* values of reference HOA and OOA reported by Ng et al. [21]. Nevertheless, our data exhibit a slightly lower *f43* value as compared to the reference data. Since *f43* represents the organic fraction of the *m/z 43* ion over the total organic, this UMR analysis fails to perfectly discern the contribution of hydrocarbons from oxygenates. Indeed, the *f43* can be attributed either to oxygenated species or hydrocarbon ones. Therefore, in the following paragraph, the high-resolution analysis is also described.

Based on the high-resolution ToF-AMS data it was possible to plot the Van Krevelen diagrams that show the H:C vs O:C. In the plot, shown in Fig. 9, further information can be extracted to better characterize the chemical composition of the aerosol. The straight black lines separate different regions in which the main oxygenated functional groups are located. The lines are labeled as "m", where "m" corresponds to the angular coefficient, hence the slope, of each line. The slopes m = 0, 1, 2 stand for alcohol/peroxides, carboxylic acids, and ketone/aldehydes functional groups, respectively. Different carbon oxidation states are represented on the plot by the positive-slope grey dashed lines. Generally, the oxidation state (OS) of an atom is defined as its formal charge assigned, assuming the atom loses its valence electrons to the most electronegative element when a molecule is formed. The OS will necessarily increase in oxidizing environments, such as the Earth's atmosphere [64]. The equation used to calculate the OS is reported in the supplemental material. The area bordered by the blue and red dashed lines, representing the lower and upper limit of the region respectively, is correlated to the triangular region present in the *f43* vs *f44* plot. As for the triangular plot, atmospheric samples of OA components generally fall inside the area. Further information about this correlation is reported in the supplemental material. The analysis of these plots contributes to better identifying the chemical species formed during the photo-oxidation of the samples. As for the pie charts reported in the 3.3 paragraph, the $C_2H_4^+$ ion was not included in the fitting procedure.

Fig. 9 reports Van Krevelen plots for the three-residence time in flame with an [O_3] equal to 0 and 5 ppm.

The oxidative environment produces a visible increase in the O:C ratio across all the experimental conditions and a reduction in the H:C ratio, congruent with our previous findings during the analysis of organic fractions. Furthermore, OOA compounds are observed to form within oxidative conditions. In addition, it is remarkable that in this more sensible analysis, the OOA data fall in the triangular region.

The OS of the compounds undergoes an increment, approximating from an average value of −1.5 to an average value of −0.85, attributable to the presence of more oxygenated species. The rise in organic aerosol (OA) secondary formation was likely attributed to heterogeneous oxidation processes. The observed alterations align closely with previous findings regarding aromatic precursors and with observations of OA transformations under photochemical conditions [21,65]. The results presented in Fig. 9 were compared with the main literature data available in the HR-AMS spectral database [66,67]. Specifically, the H:C and O:C data of the ambient components (HOA and OOA) were provided in Table S1 by Canagaratna et al. [68]; here are reported the studies [69–81]. The robustness of our study's findings is reinforced by the alignment observed between our data and those reported in the literature, both for the unoxidized conditions, in line with the HOA data, and for the oxidized conditions in line with the OOA data, as evidenced by the comparison in Fig. 9. This result means that, even by a laboratory experimental setup, secondary aerosol species are obtained with chemical characteristics closely resembling those found in the ambient. This, in turn, lays the way for future and more comprehensive investigations into primary and secondary aerosol formation by using laboratory flame aerosol generators combined with oxidation flow reactors.

4. Conclusions

In this study, a detailed investigation of the SOA formation simulating an aging period of approximately 2 days is proposed. To perform this study, the characterization of the vapors and soot particles produced

by a combustion system, i.e. an ethylene–air flame, was performed through particle size distribution functions and mass spectra analysis.

The PSD analysis highlighted the formation of new and larger particles as a consequence of the photo-oxidation process. At high residence time in flame ($H = 14$ mm) an additional mode with particles of intermediate size equal to 6 nm is registered when the photo-oxidation is induced.

The mass spectrometry investigation unveiled significant changes in SOA with respect to POA, marked by a reduction and, in some cases, the disappearance of specific peaks. Since almost all signals fall in the 10–120 m/z range, a high-resolution analysis was required. Our findings show that CH-like hydrocarbon species have the most significant influence on POA. Further POA-oriented analysis reveals that also a small fraction of CHO_{gt1} and CHO is present. The outcomes highlight a conspicuous increase in the presence of oxygenated carbon compounds significantly contributing to the formation of SOA. Thereby, CH contributions are reduced. The C_x species, associated with fullerenes generation, show an increasing contribution following the residence time in flame but with no crucial variation in the oxidized condition. Conversely, the contribution of nitrogen species, while present, remained relatively contained. Investigations based on triangular plots and the Van Krevelen diagrams allow us to validate the observed oxidation trends. However, in this laboratory study it emerges that triangular plots are not the most suitable tool for evaluating oxidative trends. Van Krevelen diagrams, performed through high resolution mode better discern the contribution of oxygenated and hydrocarbon species. This analysis suggests that a promotion in the oxygenated compounds formation happens by photo-oxidation simultaneously with a reduction of the hydrocarbon-like species. The trends agree with the formation of oxidized species, particularly carboxylic acids. Therefore, the data analysed in this study could represent a starting point for the evaluation of SOA generation and characterization by using laboratory flame aerosol generators combined with oxidation flow reactors, with the possibility of being implemented also in atmospheric studies.

CRediT authorship contribution statement

Fabio Sasso: Writing – original draft, Visualization, Investigation, Formal analysis, Conceptualization. **Francesca Picca:** Writing – original draft, Visualization, Investigation, Formal analysis, Conceptualization. **Alessia Pignatelli:** Writing – original draft, Visualization, Investigation, Formal analysis, Conceptualization. **Mario Commodo:** Writing – review & editing, Visualization, Validation, Supervision. **Patrizia Minutolo:** Writing – review & editing, Visualization, Validation, Supervision. **Andrea D'Anna:** Writing – review & editing, Visualization, Validation, Supervision, Project administration, Funding acquisition.

Declaration of competing interest

The authors declare that they have no known competing financial interests or personal relationships that could have appeared to influence the work reported in this paper.

Data availability

Data will be made available on request.

Acknowledgements

This work was supported by FESR PIR057_00015 PER-ACTRIS-IT "Potenziamento della componente italiana della Infrastruttura di Ricerca Aerosol, Clouds and Trace Gases Research Infrastructure", by the project CIR – "Capitale Umano delle Infrastrutture di Ricerca di ACTRIS", by the project ITINERIS–Italian Integrated Environmental Research Infrastructures System, by PRIN– "Investigating atmospheric fate and Toxicological properties of Biofuels Emitted ultrafine particles with a SimulaTion chamber (IT-BEST)".

Appendix A. Supplementary material

Supplementary data to this article can be found online at https://doi.org/10.1016/j.fuel.2024.131491.

References

[1] Randall D, Artaxo P, Bretherton C, Feingold G, Forster P, Kerminen V, et al. Clouds and Aerosols. In: Climate Change 2013: The Physical Science Basis. Contribution of Working Group I to the Fifth Assessment Report of the Intergovernmental Panel on Climate Change Coordinating Lead Authors: Lead Authors. 2013.
[2] Li Z, Rosenfeld D, Fan J. Aerosols and Their Impact on Radiation, Clouds, Precipitation, and Severe Weather Events. Oxford Research Encyclopedia of Environmental Science, Oxford University Press; 2017. doi: 10.1093/acrefore/9780199389414.013.126.
[3] Zhao A, Bollasina MA, Crippa M, Stevenson DS. Significant climate impacts of aerosol changes driven by growth in energy use and advances in emissions control technology. Atmos Chem Phys 2019;19:14517–33. https://doi.org/10.5194/acp-2019-616.
[4] Charlson RJ, Schwartz SE, Hales JM, Cess RD, Coakley JA, Hansen JE, et al. Climate forcing by anthropogenic aerosols. Science 1979;1992(255):423–30. https://doi.org/10.1126/science.255.5043.423.
[5] Oh H-J, Ma Y, Kim J. Human inhalation exposure to aerosol and health effect: Aerosol monitoring and modelling regional deposited doses. Int J Environ Res Public Health 2020;17:1923. https://doi.org/10.3390/ijerph17061923.
[6] Manisalidis I, Stavropoulou E, Stavropoulos A, Bezirtzoglou E. Environmental and health impacts of air pollution: A review. Front Public Health 2020;20(8):14. https://doi.org/10.3389/fpubh.2020.00014.
[7] Contini D, Lin Y-H, Hänninen O, Viana M. Contribution of aerosol sources to health impacts. Atmos 2021;12:730. https://doi.org/10.3390/atmos12060730.
[8] Lee JT. Review of epidemiological studies on air pollution and health effects in children. Clin Exp Pediatr 2021;64:3–11. https://doi.org/10.3345/cep.2019.00843.
[9] Su H, Cheng Y, Pöschl U. New multiphase chemical processes influencing atmospheric aerosols, air quality, and climate in the anthropocene. Acc Chem Res 2020;53:2034–43. https://doi.org/10.1021/acs.accounts.0c00246.
[10] Wayne RP. Chemistry of atmospheres. United States: 1985.
[11] Pryor SC, Crippa P, Sullivan RC. Atmospheric Chemistry. Reference Module in Earth Systems and Environmental Sciences, Elsevier; 2015. doi: 10.1016/B978-0-12-409548-9.09177-6.
[12] Bond TC, Scott CE. Aerosol and precursor gas emissions. Aerosol Clim 2022: 299–342. https://doi.org/10.1016/B978-0-12-819766-0.00006-7.
[13] Jimenez JL; CMR; DNM; PASH; ZQ; KJH; DPF; AJD; CH; NNL; et al. Evolution of organic aerosols in the atmosphere. Science (1979) 2009;326:1525–9.
[14] Heald CL, Kroll JH, Jimenez JL, Docherty KS, Decarlo PF, Aiken AC, et al. A simplified description of the evolution of organic aerosol composition in the atmosphere. Geophys Res Lett 2010:37. https://doi.org/10.1029/2010GL042737.
[15] De Gouw J, Jimenez JL. Organic aerosols in the Earth's atmosphere. Environ Sci Technol 2009;43:7614–8. https://doi.org/10.1021/es9006004.
[16] Matos JTV, Duarte RMBO, Lopes SP, Silva AMS, Duarte AC. Persistence of urban organic aerosols composition: Decoding their structural complexity and seasonal variability. Environ Pollut 2017;231:281–90. https://doi.org/10.1016/J.ENVPOL.2017.08.022.
[17] Takegawa N, Miyakawa T, Kondo Y, Jimenez JL, Zhang Q, Worsnop DR, et al. Seasonal and diurnal variations of submicron organic aerosol in Tokyo observed using the aerodyne aerosol mass spectrometer. J Geophys Res Atmos 2006:111. https://doi.org/10.1029/2005JD006515.
[18] Zhang Q, Jimenez JL, Canagaratna MR, Allan JD, Coe H, Ulbrich I, et al. Ubiquity and dominance of oxygenated species in organic aerosols in anthropogenically-influenced northern hemisphere midlatitudes. Geophys Res Lett 2007:34. https://doi.org/10.1029/2007GL029979.
[19] Donahue NM, Robinson AL, Pandis SN. Atmospheric organic particulate matter: From smoke to secondary organic aerosol. Atmos Environ 2009;43:94–106. https://doi.org/10.1016/j.atmosenv.2008.09.055.
[20] Zhang Q, Rami Alfarra M, Worsnop DR, Allan JD, Coe H, Canagaratna MR, et al. Deconvolution and quantification of hydrocarbon-like and oxygenated organic aerosols based on aerosol mass spectrometry. Environ Sci Technol 2005;39:4938–52. https://doi.org/10.1021/es048568l.
[21] Ng NL, Canagaratna MR, Jimenez JL, Chhabra PS, Seinfeld JH, Worsnop DR. Changes in organic aerosol composition with aging inferred from aerosol mass spectra. Atmos Chem Phys 2011;11:6465–74. https://doi.org/10.5194/acp-11-6465-2011.
[22] Gentner DR, Jathar SH, Gordon TD, Bahreini R, Day DA, El Haddad I, et al. Review of urban secondary organic aerosol formation from gasoline and diesel motor vehicle emissions. Environ Sci Technol 2017;51:1074–93. https://doi.org/10.1021/acs.est.6b04509.
[23] Tkacik et Al. Secondary organic aerosol formation from in-use motor vehicle emissions using a potential aerosol mass reactor. Environ, Sci, Technol 2014;48:11235–42.

[24] Srivastava D, Vu T V, Tong S, Shi Z, Harrison RM. Formation of secondary organic aerosols from anthropogenic precursors in laboratory studies n.d. doi: 10.1038/s41612-022-00238-6.
[25] Hooftman N, Messagie M, Van Mierlo J, Coosemans T. A review of the European passenger car regulations – Real driving emissions vs local air quality. Renew Sustain Energy Rev 2018;86:1–21. https://doi.org/10.1016/J.RSER.2018.01.012.
[26] Morino Y, Li Y, Fujitani Y, Sato K, Inomata S, Tanabe K, et al. Secondary organic aerosol formation from gasoline and diesel vehicle exhaust under light and dark conditions. Environ Sci: Atmos 2022;2:46–64. https://doi.org/10.1039/D1EA00045D.
[27] Chirico et al. Impact of aftertreatment devices on primary emissions and secondary organic aerosol formation potential from in-use diesel vehicles: results from smog chamber experiments. Atmos Chem Phys 2010;10:11545–63.
[28] Pieber et al. A. Gas-phase composition and secondary organic aerosol formation from standard and particle filter-retrofitted gasoline direct injection vehicles investigated in a batch and flow reactor. Atmos Chem Phys 2018;18:9929–54.
[29] Timonen et al. Influence of fuel ethanol content on primary emissions and secondary aerosol formation potential for a modern flex-fuel gasoline vehicle. Atmos Chem Phys 2017;17:5311–29.
[30] Bahreini R, Middlebrook AM, De Gouw JA, Warneke C, Trainer M, Brock CA, et al. Gasoline emissions dominate over diesel in formation of secondary organic aerosol mass. Geophys Res Lett 2012:39. https://doi.org/10.1029/2011GL050718.
[31] Cifuentes F, González CM, Trejos EM, López LD, Sandoval FJ, Cuellar OA, et al. Comparison of Top-Down and Bottom-Up Road Transport Emissions through High-Resolution Air Quality Modeling in a City of Complex Orography 2021. doi: 10.3390/atmos12111372.
[32] Suarez et al. Primary emissions and secondary organic aerosol formation from the exhaust of a flex-fuel (ethanol) vehicle. Atmos Environ 2015;117:200–11.
[33] Simonen P, Saukko E, Karjalainen P, Timonen H, Bloss M, Aakko-Saksa P, et al. A new oxidation flow reactor for measuring secondary aerosol formation of rapidly changing emission sources. Atmos Meas Tech 2017;10:1519–37. https://doi.org/10.5194/amt-10-1519-2017.
[34] Leone JA, Flagan RC, Grosjean D, Seinfeld JH. An outdoor smog chamber and modeling study of toluene–NO $_x$ photooxidation. Int J Chem Kinet 1985;17:177–216. https://doi.org/10.1002/kin.550170206.
[35] Wang J, Doussin JF, Perrier S, Perraudin E, Katrib Y, Pangui E, et al. Design of a new multi-phase experimental simulation chamber for atmospheric photosmog, aerosol and cloud chemistry research. Atmos Meas Tech 2011;4:2465–94. https://doi.org/10.5194/amt-4-2465-2011.
[36] Presto AA, Huff Hartz KE, Donahue NM. Secondary organic aerosol production from terpene ozonolysis. 2. Effect of NO $_x$ concentration. Environ Sci Technol 2005;39:7046–54. https://doi.org/10.1021/es050400s.
[37] Edney EO, Driscoll DJ, Weathers WS, Kleindienst TE, Conver TS, McIver CD, et al. Formation of polyketones in irradiated toluene/propylene/NOx/Air mixtures. Aerosol Sci Tech 2001;35:998–1008. https://doi.org/10.1080/02786820173306769.
[38] Bin LY, Ziemann PJ. Chemistry of secondary organic aerosol formation from OH radical-initiated reactions of linear, branched, and cyclic alkanes in the presence of NO. Aerosol Sci Tech 2009;43:604–19. https://doi.org/10.1080/02786820902802567.
[39] Chu B, Chen T, Liu Y, Ma Q, Mu Y, Wang Y, et al. Application of smog chambers in atmospheric process studies. Natl Sci Rev 2022;9. https://doi.org/10.1093/nsr/nwab103.
[40] Xu N, Collins DR. Design and characterization of a new oxidation flow reactor for laboratory and long-term ambient studies. Atmos Meas Tech 2021;14:2891–906. https://doi.org/10.5194/amt-14-2891-2021.
[41] Kuittinen N, McCaffery C, Peng W, Zimmerman S, Roth P, Simonen P, et al. Effects of driving conditions on secondary aerosol formation from a GDI vehicle using an oxidation flow reactor. Environ Pollut 2021;282. https://doi.org/10.1016/j.envpol.2021.117069.
[42] Simonen P, Kalliokoski J, Karjalainen P, Rönkkö T, Timonen H, Saarikoski S, et al. Characterization of laboratory and real driving emissions of individual Euro 6 light-duty vehicles – Fresh particles and secondary aerosol formation. Environ Pollut 2019;255. https://doi.org/10.1016/j.envpol.2019.113175.
[43] Peng Z, Jimenez JL. Radical chemistry in oxidation flow reactors for atmospheric chemistry research. Chem Soc Rev 2020;49:2570–616. https://doi.org/10.1039/C9CS00766K.
[44] Zhao B, Yang Z, Wang J, Johnston MV, Wang H. Analysis of soot nanoparticles in a laminar premixed ethylene flame by scanning mobility particle sizer. Aerosol Sci Tech 2003;37:611–20. https://doi.org/10.1080/02786820300908.
[45] Zhao B, Yang Z, Johnston MV, Wang H, Wexler AS, Balthasar M, et al. Measurement and numerical simulation of soot particle size distribution functions in a laminar premixed ethylene-oxygen-argon flame. Combust Flame 2003;133:173–88. https://doi.org/10.1016/S0010-2180(02)00574-6.
[46] Sgro LA, Basile G, Barone AC, D'Anna A, Minutolo P, Borghese A, et al. Detection of combustion formed nanoparticles. Chemosphere 2003;51:1079–90. https://doi.org/10.1016/S0045-6535(02)00718-X.
[47] Sabbah H, Commodo M, Picca F, De Falco G, Minutolo P, D'Anna A, et al. Molecular content of nascent soot: Family characterization using two-step laser desorption laser ionization mass spectrometry. Proc Combust Inst 2021;38:1241–8. https://doi.org/10.1016/j.proci.2020.09.022.
[48] Reischl GP, Makehi JM, Karch R, Necid J. Bipolar charging of ultrafine particles in the size range below 10 nm. J Aerosol Sci 1996:931–49. https://doi.org/10.1016/0021-8502(96)00026-2.
[49] Commodo M, De Falco G, Bruno A, Borriello C, Minutolo P, D'Anna A. Physicochemical evolution of nascent soot particles in a laminar premixed flame: From nucleation to early growth. Combust Flame 2015;162:3854–63. https://doi.org/10.1016/j.combustflame.2015.07.022.
[50] Cereceda-Balic F, Toledo M, Vidal V, Guerrero F, Diaz-Robles LA, Petit-Breuilh X, et al. Emission factors for PM2.5, CO, CO2, NOx, SO2 and particle size distributions from the combustion of wood species using a new controlled combustion chamber 3CE. Sci Total Environ 2017;584–585:901–10. https://doi.org/10.1016/J.SCITOTENV.2017.01.136.
[51] Xu W, Croteau P, Williams L, Canagaratna M, Onasch T, Cross E, et al. Laboratory characterization of an aerosol chemical speciation monitor with PM2.5 measurement capability. Aerosol Sci Tech 2017;51:69–83. https://doi.org/10.1080/02786826.2016.1241859.
[52] Canagaratna MR, Jayne JT, Jimenez JL, Allan JD, Alfarra MR, Zhang Q, et al. Chemical and microphysical characterization of ambient aerosols with the aerodyne aerosol mass spectrometer. Mass Spectrom Rev 2007;26:185–222. https://doi.org/10.1002/mas.20115.
[53] DeCarlo PF, Kimmel JR, Trimborn A, Northway MJ, Jayne JT, Aiken AC, et al. Field-deployable, high-resolution, time-of-flight aerosol mass spectrometer. Anal Chem 2006;78:8281–9. https://doi.org/10.1021/ac061249n.
[54] Echavarria CA, Sarofim AF, Lighty JS, D'Anna A. Modeling and measurements of size distributions in premixed ethylene and benzene flames. Proc Combust Inst.2009;32 I:705–11. doi: 10.1016/j.proci.2008.06.172.
[55] Sirignano M, Kent J, D'Anna A. Modeling formation and oxidation of soot in nonpremixed flames. Energy Fuel 2013;27:2303–15. https://doi.org/10.1021/ef400057r.
[56] He LY, Lin Y, Huang XF, Guo S, Xue L, Su Q, et al. Characterization of high-resolution aerosol mass spectra of primary organic aerosol emissions from Chinese cooking and biomass burning. Atmos Chem Phys 2010;10:11535–43. https://doi.org/10.5194/acp-10-11535-2010.
[57] Aiken AC, DeCarlo PF, Jimenez JL. Elemental analysis of organic species with electron ionization high-resolution mass spectrometry. Anal Chem 2007;79:8350–8. https://doi.org/10.1021/ac071150w.
[58] Zhu W, Guo S, Zhang Z, Wang H, Yu Y, Chen Z, et al. Mass spectral characterization of secondary organic aerosol from urban 1 cooking and vehicular sources. Atmos Chem Phys 2021;21:15065–79.
[59] Heringa MF, Decarlo PF, Chirico R, Tritscher T, Clairotte M, Mohr C, et al. A new method to discriminate secondary organic aerosols from different sources using high-resolution aerosol mass spectra. Atmos Chem Phys 2012;12:2189–203. https://doi.org/10.5194/acp-12-2189-2012.
[60] Craven JS, Yee LD, Ng NL, Canagaratna MR, Loza CL, Schilling KA, et al. Analysis of secondary organic aerosol formation and aging using positive matrix factorization of high-resolution aerosol mass spectra: application to the dodecane low-NO$_x$ system. Atmos Chem Phys 2012;12:11795–817. https://doi.org/10.5194/acp-12-11795-2012.
[61] Alfarra MR, Paulsen D, Gysel M, Garforth AA, Dommen J, Prévôt ASH, et al. Atmospheric Chemistry and Physics A mass spectrometric study of secondary organic aerosols formed from the photooxidation of anthropogenic and biogenic precursors in a reaction chamber. Atmos Chem Phys 2006; 6: 5279–5293.
[62] Roberts VJD, Caserio MC. Basic Principles of Organic Chemistry. New York: 1964.
[63] Ng NL, Canagaratna MR, Zhang Q, Jimenez JL, Tian J, Ulbrich IM, et al. Organic aerosol components observed in northern hemispheric datasets from aerosol mass spectrometry. Atmos Chem Phys 2010;10:4625–41. https://doi.org/10.5194/acp-10-4625-2010.
[64] Kroll JH, Donahue NM, Jimenez JL, Kessler SH, Canagaratna MR, Wilson KR, et al. Carbon oxidation state as a metric for describing the chemistry of atmospheric organic aerosol. Nat Chem 2011;3:133–9. https://doi.org/10.1038/nchem.948.
[65] Lambe AT, Onasch TB, Massoli P, Croasdale DR, Wright JP, Ahern AT, et al. Laboratory studies of the chemical composition and cloud condensation nuclei (CCN) activity of secondary organic aerosol (SOA) and oxidized primary organic aerosol (OPOA). Atmos Chem Phys 2011;11:8913–28. https://doi.org/10.5194/acp-11-8913-2011.
[66] Ulbrich IM, Canagaratna MR, Zhang Q, Worsnop DR, Jimenez JL. Interpretation of organic components from positive matrix factorization of aerosol mass spectrometric data. Atmos Chem Phys 2009;9:2891–918. https://doi.org/10.5194/acp-9-2891-2009.
[67] High Resolution AMS Spectral Database. http://cires.colorado.edu/jimenez-group/HRAMSsd/ n.d.
[68] Canagaratna MR, Jimenez JL, Kroll JH, Chen Q, Kessler SH, Massoli P, et al. Elemental ratio measurements of organic compounds using aerosol mass spectrometry: Characterization, improved calibration, and implications. Atmos Chem Phys 2015;15:253–72. https://doi.org/10.5194/acp-15-253-2015.
[69] He L-Y, Huang X-F, Xue L, Hu M, Lin Y, Zheng J, et al. Submicron aerosol analysis and organic source apportionment in an urban atmosphere in Pearl River Delta of China using high-resolution aerosol mass spectrometry. J Geophys Res 2011;116:D12304. https://doi.org/10.1029/2010JD014566.
[70] Aiken AC, Salcedo D, Cubison MJ, Huffman JA, DeCarlo PF, Ulbrich IM, et al. Mexico City aerosol analysis during MILAGRO using high resolution aerosol mass spectrometry at the urban supersite (T0) – Part 1: Fine particle composition and organic source apportionment. Atmos Chem Phys 2009;9:6633–53. https://doi.org/10.5194/acp-9-6633-2009.
[71] DeCarlo PF, Ulbrich IM, Crounse J, de Foy B, Dunlea EJ, Aiken AC, et al. Investigation of the sources and processing of organic aerosol over the central Mexican plateau from aircraft measurements during MILAGRO. Atmos Chem Phys 2010;10:5257–80. https://doi.org/10.5194/acp-10-5257-2010.
[72] Docherty KS, Aiken AC, Huffman JA, Ulbrich IM, DeCarlo PF, Sueper D, et al. The 2005 study of organic aerosols at riverside (SOAR-1): Instrumental

intercomparisons and fine particle composition. Atmos Chem Phys 2011;11:12387–420. https://doi.org/10.5194/acp-11-12387-2011.
[73] Ge X, Setyan A, Sun Y, Zhang Q. Primary and secondary organic aerosols in Fresno, California during wintertime: Results from high resolution aerosol mass spectrometry. J Geophys Res Atmos 2012;117. https://doi.org/10.1029/2012JD018026.
[74] Gong Z, Lan Z, Xue L, Zeng L, He L, Huang X. Characterization of submicron aerosols in the urban outflow of the central Pearl River Delta region of China. Front Environ Sci Eng 2012;6:725–33. https://doi.org/10.1007/s11783-012-0441-8.
[75] Wang X, Gao S, Yang X, Chen H, Chen J, Zhuang G, et al. Evidence for high molecular weight nitrogen-containing organic salts in urban aerosols. Environ Sci Technol 2010;44:4441–6. https://doi.org/10.1021/es1001117.
[76] Huang X-F, He L-Y, Xue L, Sun T-L, Zeng L-W, Gong Z-H, et al. Highly time-resolved chemical characterization of atmospheric fine particles during 2010 Shanghai world expo. Atmos Chem Phys 2012;12:4897–907. https://doi.org/10.5194/acp-12-4897-2012.
[77] Huang X-F, Xue L, Tian X-D, Shao W-W, Sun T-L, Gong Z-H, et al. Highly time-resolved carbonaceous aerosol characterization in Yangtze River Delta of China: Composition, mixing state and secondary formation. Atmos Environ 2013;64:200–7. https://doi.org/10.1016/j.atmosenv.2012.09.059.
[78] Mohr C, DeCarlo PF, Heringa MF, Chirico R, Slowik JG, Richter R, et al. Identification and quantification of organic aerosol from cooking and other sources in Barcelona using aerosol mass spectrometer data. Atmos Chem Phys 2012;12:1649–65. https://doi.org/10.5194/acp-12-1649-2012.
[79] Saarikoski S, Carbone S, Decesari S, Giulianelli L, Angelini F, Canagaratna M, et al. Chemical characterization of springtime submicrometer aerosol in Po Valley. Italy Atmos Chem Phys 2012;12:8401–21. https://doi.org/10.5194/acp-12-8401-2012.
[80] Setyan A, Zhang Q, Merkel M, Knighton WB, Sun Y, Song C, et al. Characterization of submicron particles influenced by mixed biogenic and anthropogenic emissions using high-resolution aerosol mass spectrometry: results from CARES. Atmos Chem Phys 2012;12:8131–56. https://doi.org/10.5194/acp-12-8131-2012.
[81] Sun Y-L, Zhang Q, Schwab JJ, Demerjian KL, Chen W-N, Bae M-S, et al. Characterization of the sources and processes of organic and inorganic aerosols in New York city with a high-resolution time-of-flight aerosol mass apectrometer. Atmos Chem Phys 2011;11:1581–602. https://doi.org/10.5194/acp-11-1581-2011.